Check for updates

Design of SrTiO₃-based catalysts for photocatalytic CO₂ reduction†

Bíborka Boga,[ab] Nikolaos G. Moustakas,[a] Yunyan Han,[ac] Haijun Jiao, [iD][a] Carsten Kreyenschulte, [iD][a] Pawel Naliwajko,[a] Thi Thanh Hoa Duong,[a] Shuoping Ding, [iD][a] Anh Binh Ngo,[a] Abdo Hezam,[d] Tim Peppel, [iD][a] Vasile-Mircea Cristea, [iD][b] Norbert Steinfeldt [iD]*[a] and Jennifer Strunk [iD]*[ad]

Herein, the preparation of SrTiO₃-based catalysts (*i.e.*, NiO/support, Au-support and Au–NiO/support, where the supports were SrTiO₃ and SrTiO₃–SrCO₃) for photocatalytic CO₂ reduction considering strategic design principles is presented. The samples were comprehensively analyzed *via* complementary methods, such as SEM-EDX, XRD, nitrogen sorption, XPS and UV-vis (DRS), *in situ* EPR and *in situ* DRIFTS. The CO₂ photoreduction activity of the samples was assessed in a high-purity gas-phase photoreactor under batch conditions. The investigations highlighted that the reaction pathway (*i.e.*, selective H₂ and C₂H₆ production *vs.* CH₄) can be influenced by the modification of the electronic properties (*i.e.*, Fermi level alignment), the interaction between Au NPs and oxygen vacancies (*i.e.*, *in situ* EPR) and the enhanced charge separation in the presence of SrCO₃. The participation of the structural carbonates in the reaction in association with the functionality of the components is discussed.

Introduction

The photocatalytic conversion of CO₂ into valuable fuels (CH₄ or higher hydrocarbons) over metal oxide-based catalysts is a smart and promising solution for overcoming the problem of increasing atmospheric CO₂ concentration (425 ppm[1]) and energy demand.[2]

Perovskites, also called "chameleon CO₂ photocatalysts"[3] are very interesting for such applications owing to multiple reasons. Among them, SrTiO₃ has received considerable attention in this field, *e.g.*, Ti-rich and Sr(OH)₂-decorated SrTiO₃,[4] boron-doped layered polyhedron SrTiO₃,[5] or SnS₂-decorated 3DOM-SrTiO₃.[6] Their impressive photocatalytic performance was mainly attributed to its advantageous band structure, more precisely its conduction band (CB) minimum edge position. Recently, studies aiming at the study of self-doped SrTiO₃₋δ,[7] "black SrTiO₃",[8] and SrTiO₃

with crystalline core/amorphous shell structure (*i.e.*, SrTiO₃@SrTiO₃₋ₓ)[9] were conducted for photocatalytic CO₂ reduction applications.

Although heterostructures formed from metal oxides possess several promising features, the coupling of metal nanoparticles with metal oxides provides additional positive aspects for both catalytic and photocatalytic applications. In the latter case, both the material/type of the metal nanoparticle, and its morphology and distribution are critical factors. Considerable importance was given to noble metal (*i.e.*, Au, Ru, Pt, Pd) catalysts on supports in photocatalytic CO₂ reduction applications.[10] Among these, supported Au-catalysts received remarkable attention (*i.e.*, Au/TiO₂,[11,12] Au/ZnO[13]) due to their enhanced visible light activity, mostly explained by the localized plasmon resonance effect of Au nanoparticles or due to Au interband transitions (hot electrons in Au/SrTiO₃ systems).[14] Regardless of the advantageous electronic features of SrTiO₃, *i.e.*, the optimal Schottky barrier height, in coupling with Au or Ag (*i.e.*, in the case of Au–SrTiO₃, = 1–1.5 eV[15,16]),[17] a relatively small number of studies have focused on the study of (plasmonic) metal-SrTiO₃ heterostructures (Ag/SrTiO₃ (ref. 18)).

Beyond the previously discussed trivial aspects related to metal NPs (morphology and distribution), the metal/support interface must also be considered, since it governs the efficiency of interfacial electron transfer and the charge dynamics.[17,19] Moreover, since not only the charge transfer

[a] Leibniz Institute for Catalysis e.V. (LIKAT), Albert Einstein St., 29.A, Rostock, 18059, Germany. E-mail: Norbert.Steinfeldt@catalysis.de

[b] Faculty of Chemistry and Chemical Engineering, Babes-Bolyai University, Arany Janos St, 11, Cluj-Napoca, 400028, Romania

[c] Shaanxi Key Laboratory of Phytochemistry, College of Chemistry & Chemical Engineering, Baoji University of Arts and Sciences, Baoji 721013, China

[d] Industrielle Chemie und Heterogene Katalyse, Technical University of Munich (TUM), Lichtenberg St, 4, Munich, 85745, Germany. E-mail: Jennifer.Strunk@tum.de

† Electronic supplementary information (ESI) available. See DOI: https://doi.org/10.1039/d4cy00313f

This journal is © The Royal Society of Chemistry 2024

Catal. Sci. Technol., 2024, **14**, 3459–3472 | **3459**

but also the reaction can occur at the interface, its active sites must also be taken into account.[17] The selected preparation method influences considerably the interfacial electronic structure, as for example, the quantity of the interfacial defects (Ti^{3+} centers), which act as electron traps, thus inhibiting the interfacial electron transfer in Au/TiO_2 systems.[12]

In this work, the effect of NiO impregnation or/and Au-photodeposition on different $SrTiO_3$-supports has been studied in association with the assessment of their photocatalytic CO_2 reduction activity and their light-induced CO_2 adsorption ability. As supports, commercial $SrTiO_3$, commercial $SrCO_3$, and $SrTiO_3$–$SrCO_3$ prepared by hydrothermal crystallization were employed. To the best of our knowledge, the combination of the aforementioned components, namely NiO, Au, $SrTiO_3$ and $SrCO_3$, has not been previously studied in the literature. Additional motivating points of our work are related to the fact that, despite its potential, a relatively small number of studies are dealing with $SrTiO_3$–$SrCO_3$ in photocatalytic CO_2 reduction applications[20] (it is mainly used for photooxidation of NO,[21] CH_4,[22] and degradation of active pharmaceutical ingredients[23]), and that the effect of structural carbonates is still a matter of debate in photocatalytic CO_2 reduction (e.g., TiO_2,[24] ZnO[25]).

Experimental

Chemicals

The chemicals for synthesis and analysis: strontium nitrate ($Sr(NO_3)_2$, Sigma Aldrich, Germany, ≥99%), titanium(IV) oxide (anatase TiO_2, 10–25 nm, Iolitec, Germany, 99.5%), potassium hydroxide (KOH, Sigma Aldrich, Germany, ≥85%), nickel nitrate hexahydrate ($Ni(NO_3)_2 \cdot 6H_2O$, Merck, Germany, ACS), hydrogen tetrachloridoaurate(III) trihydrate ($HAuCl_4 \cdot 3H_2O$, ABCR, Germany, 99.99%), ethanol (Merck, Germany, >99%), isopropanol (Merck, Germany, 99.9%) were used without any preliminary purification. The reference support materials were $SrTiO_3$ (Iolitec, Germany, 99.99%) and $SrCO_3$ (Merck, Germany, 99.99%).

Preparation of the studied materials

Preparation of the supports

Optimized support. 1.428 g (6.748 mmoles) $Sr(NO_3)_2$ was dissolved in 70 ml distilled H_2O under continuous stirring (500 rpm), followed by the addition of 0.479 g (5.999 mmoles) anatase TiO_2 into the reaction mixture, thus assuring an excess of 12.5% (molar) of Sr^{2+}. The as-prepared reaction mixture was ultrasonicated for 3 min. After the stepwise addition of 31.419 g (0.560 moles) KOH, the reaction mixture was stirred for 30 min (500 rpm), and hydrothermally treated at 180 °C over 12 h in a PTFE-lined autoclave. The precipitate was washed once with EtOH and 3 times with distilled H_2O, followed by drying in air (80 °C, 12 h). Considering the elemental

analysis (EA) results, namely 1.1 wt% C content of the support, which led to the overall ~18 wt% of $SrCO_3$ in the final product. The final mass of the product after the synthesis was 1.165 g, which resulted in a yield of 87%. The support was denoted as STO-SCO (HT).

Reference support. Since commercial $SrTiO_3$ and commercial $SrCO_3$ were considered as reference supports, the composite consisting of commercial $SrTiO_3$ and $SrCO_3$ (in the same content as the hydrothermally synthesized sample) was prepared via the suspension method. More precisely, 0.656 g $SrTiO_3$ and 0.144 g $SrCO_3$ were introduced into 30 mL H_2O, and was kept under stirring for 1 h, followed by drying at 80 °C over 12 h. The as-prepared sample is denoted as STO-SCO (SM). The commercial supports were denoted as STO and SCO, respectively.

Impregnation of the support with NiO

To favor the adsorption of CO_2 on the $SrTiO_3$-based support, one promising option is the modification of the surface of a catalyst with transition metal oxides to render its surface more basic (i.e., NiO with PZC: 8–9 (ref. 26)). The impregnation of STO-SCO (HT) or STO was similar to what was previously reported in the literature.[27] 12.13 mg (0.066 mmoles) $Ni(NO_3)_2 \cdot 6H_2O$ was dissolved in 30 ml distilled H_2O, followed by the addition of 0.800 g support (either STO-SCO (HT) or STO). The as-prepared suspension was stirred for 1 h (500 rpm) and centrifuged, and the obtained solid was washed once with EtOH, 3 times with distilled H_2O and dried in air (180 °C, 12 h). Finally, calcination of the sample was performed in a static air atmosphere at 700 °C for 4 h. The nominal content of NiO was 0.3 wt%, which was in accordance with the experimentally determined Ni^{2+} content (±5% relative error).

Au photodeposition

The Au-photodeposition was performed according to a method described previously[12,28] involving (1) pre-irradiation of 10 mL 0.594 mM ethanolic $HAuCl_4$ solution and catalyst suspension over 10 min; (2) dropwise addition of 10 mL $HAuCl_4$ solution over the catalyst suspension; (3) irradiation of the mixture over 15 minutes. The washing was performed with distilled H_2O and centrifugation, followed by drying at 90 °C in air for 16 h. The experimentally determined Au content (error ±10%, theoretical Au content: 1 wt%) of the samples was in accordance with the expected/theoretical Au content.

Remark: Since studies were already conducted to investigate the influence of Au content on the photocatalytic activity of $SrTiO_3$-based samples (e.g., 1.1 wt% Au nanospheres over $SrTiO_3$ via precipitation–deposition,[14] 1 wt% Au microspheres over $SrTiO_3/TiO_2$ via photoreduction[29]), the optimized Au content recommended by results reported in the literature was considered.

3460 | *Catal. Sci. Technol.*, 2024, **14**, 3459–3472

This journal is © The Royal Society of Chemistry 2024

Material characterization

Methods

The elemental composition of the synthesized catalysts was determined by inductively coupled plasma optical emission spectroscopy (ICP-OES, Varian/Agilent 715-ES, Germany).

The assessment of morpho-structural features of the catalysts was performed based on the SEM (scanning electron microscopy) micrographs recorded using a Merlin VP compact device (Zeiss, Oberkochen, Germany).

Scanning transmission electron microscopy (STEM) provided a more detailed overview on the structural features of the selected samples using a probe aberration corrected ARM200F (Jeol, Tokyo, Japan) operated at 200 kV and equipped with high angle annular dark field (HAADF) and annular bright field (ABF) detectors and a DRY SD60GV (JEOL) energy dispersive X-ray spectrometer (EDXS). Specimens were dry deposited onto a Cu grid with a holey carbon film.

An Xpert Pro diffractometer (PANalytical, the Netherlands) equipped with a $CuK_{\alpha1}K_{\alpha2}$ radiation source (λ_1 = 0.15406 nm, λ_2 = 0.15443 nm) was used for the recording of the X-ray diffraction (XRD) patterns. The Scherrer equation was used for the calculation of the primary crystallite size.[30] The Rietveld analysis was performed in the HighScore Plus software environment.

An ESCALAB 2020iXL (Thermo Fischer Scientific) spectrometer equipped with an Al Kα radiation source was used for obtaining the results related to X-ray photoelectron spectroscopy (XPS).

The nitrogen sorption data (at 77 K) were obtained using a NOVAtouch (Quantachrome Instruments). While the Brunauer–Emmett–Teller (BET) multipoint method was considered for the determination of the specific surface area, the pore volume was extracted from the Barrett–Joyner–Halenda (BJH) data. The pre-treatment of the samples was performed via heating at 350 °C under vacuum for 5 h.

The reflectance spectra in the UV-vis range (i.e., 200–800 nm) of the studied solid catalysts were recorded using a Lambda 650 spectrophotometer (Perkin Elmer). The well-known Tauc-equation was considered for the determination of the band gap energy of $SrTiO_3$.

The paramagnetic centers of the studied $SrTiO_3$-based samples (in our case the unpaired electron in Ti^{3+} centers) were detected via in situ electron paramagnetic resonance spectroscopy (in situ EPR, Bruker EMX CW-micro X-band EPR spectrometer) under UV-vis irradiation (300 W Xe-arc lamp, LOT Oriel GmbH, Germany). The X-band EPR (serial) spectra were recorded at room temperature.

The identification of surface species involved in CO_2 adsorption was elucidated by in situ diffuse reflectance infrared Fourier transformation spectroscopy (in situ DRIFTS) (Nicolet Protégé spectrometer equipped with a Harrick HVC DRP-5 cell and Praying Mantis mirrors). Detailed description of the equipment can be found elsewhere.[24] The desired Ar and CO_2 flow rates were provided by Bronkhorst mass flow controllers (MFCs). Serial recordings were collected, with 200 scans at a resolution of 4 cm^{-1} per individual spectrum, and averaged in order to obtain the respective spectra. The studied catalyst was introduced into the reaction chamber, subsequently purged with Ar (31 mL min^{-1}) for 30 min at room temperature, followed by thermal pre-treatment aiming at the removal of surface-bound H_2O (heating rate: 10 K min^{-1} up to 400 °C, maintained at 400 °C for 60 min, natural cooling to room temperature). The CO_2 adsorption experiment was performed at room temperature under an Ar–CO_2 flow (29 mL min^{-1} Ar, 2 mL min^{-1} CO_2) over 30 min. Prior to the CO_2 adsorption experiment the as-called background spectrum was recorded, which was then subtracted from the subsequently collected spectra. The final step was purging with Ar (31 mL min^{-1}) over 1 h. The same procedure was repeated under irradiation during the CO_2 adsorption step using a Lumatec Superlite S04 lamp equipped with an optical fiber to guide the light into the chamber. Meanwhile in the first 15 min the emission was set to 320–500 nm, and during the last 15 min it was shifted to 400–700 nm with the intensity set to 25%.

A high-purity gas-phase photoreactor system was used for the assessment of the photocatalytic CO_2 reduction activity of the studied $SrTiO_3$-based samples in batch-mode. The detailed description of the experimental setup and the measurement process can be found in a recently published study from our group.[31]

Briefly, to ensure high-purity conditions, the photoreactor employed in this work is made of stainless steel and all the connections of the individual parts are performed using only metallic connectors and adaptors suitable for high pressure applications. No elastomeric parts were used to ensure that there are no products formed from the interaction of the equipment with CO_2 or from degradation of elastomeric parts under light irradiation. To exclude the formation of C-containing products from leftover surface-bound impurities from the synthesis of the photocatalysts, extensive blank experiments were performed under a humidified He environment (0.6 vol% H_2O/He) under light irradiation but in the absence of CO_2. These measurements act also as a batch cleaning process: leftover carbonaceous species are gradually removed from the surface of the samples under the influence of light. Subsequently, CO_2 photoreduction experiments have been initiated in the presence of CO_2 (1.5 vol% CO_2) and water (0.6 vol% H_2O) and He.

The experiments were performed in batch mode (initial pressure 1500 mbar) and gas samples were collected periodically (every 45 min) over a total irradiation time of 6 h. A pressure-drop correction was made to account for the removed volume in between measurements. The irradiation of the samples was performed using a 200 W Hg/Xe lamp (Newport Oriel) with a light intensity of 200 mW cm^{-2}. A water-filled IR filter was introduced in the light pathway to remove the IR region of the irradiation spectrum of the lamp and to avoid excess heat during the CO_2 reduction experiments. Gas analysis was performed using a gas

This journal is © The Royal Society of Chemistry 2024

Catal. Sci. Technol., 2024, 14, 3459–3472 | 3461

chromatograph (TRACERA-2010, Shimadzu) featuring a barrier discharge ionization detector (BID) and a flame ionization detector (FID).

The moles of the product, $n_{product}(t_i)$ expressed in µmol, at sampling time t_i were calculated following DIN SPEC91457:[32]

• Measured volume fraction of the product, $c_{product}(t_i)$, expressed in ppm, at the current sampling time t_i.

• Measured volume fractions from the previous sampling times ($c_{product}(t_j)$ where $t_j : t_1 \ldots t_{i-1}$).

• The pressure in the reactor, $p(t_i)$, $p(t_j)$, at sampling time t_i or t_j (in kPa).

• The withdrawal sample volume $V_m(t_i)$ at sampling time t_i.

• Volume of the reactor, V_R, expressed in L.

$$n_{product}(t_i) = \frac{V_R}{RT}\left(c_{product}(t_i)p(t_i) + \frac{V_m(t_i)}{V_m(t_i)+V_R} \cdot \sum_{j=1}^{t_{i-1}} c_{product}(t_j)p(t_j) \right) \quad (1)$$

The withdrawal sample volume $V_m(t_i)$ is calculated accounting the pressure drop in the reactor after sample withdrawal, as depicted in eqn (2):

$$V_m(t_i) = \left(\frac{p(t_{i-1})}{p(t_i)} - 1 \right) V_R \quad (2)$$

The products formed during the batch cleaning were subtracted from the amount of products formed during the CO_2 reduction experiments for each sampling time. The normalized concentrations were obtained by dividing the concentration of the detected products by the catalyst mass and the reaction time.

To gain insight into the mechanism of CO_2 reduction *via* $SrTiO_3$-$SrCO_3$-based materials, knowledge of the work function of $SrTiO_3$ and $SrCO_3$ and of the $SrTiO_3$-$SrCO_3$ composite is necessary. First-principles methods based on density functional theory (DFT) and density functional theory with the Hubbard U correction (DFT+U) were used for calculating the electronic properties of $SrCO_3$ and $SrTiO_3$ by using the Vienna *ab initio* simulation package (VASP).[33–35] The projected augmented wave method (PAW)[36,37] was used to describe the interaction of electrons and ions. The electron exchange and correlation energies were calculated within the generalized gradient approximation method (GGA) using the Perdew–Burke–Ernzerhof (PBE) functional.[38] Geometry optimization was converged until the forces acting on the atoms were smaller than 0.03 eV Å^{-1}, whereas the energy threshold-defining self-consistency of the electron density was set to 10^{-5} eV. The plane wave cut off was set to 520 eV in all simulations. The detailed methodology of the DFT calculations (*i.e.*, density of states of bulk $SrTiO_3$ and $SrCO_3$) is presented in the ESI† (Fig. S32 and S33†). $SrTiO_3(110)$ and $SrCO_3(111)$ slab models were built to describe the effect of the presence of new surface atoms on the position of the Fermi level. A $p(2 \times 2)$ supercell was used to simulate the clean $SrTiO_3(110)$ surface, while a $p(1 \times 1)$

supercell was used to model the $SrCO_3(111)$ surface. All models have a five-layer-deep slab, and they were allowed to fully relax without any constrains. The simulation method used required a periodic cell. In the periodic cell, a 20 Å vacuum gap was created between the upper-most and bottom-most layers. Dipolar correction in the z direction was set for all the slab models. For $SrTiO_3(110)$, the model has 20 Sr atoms, 20 Ti atoms and 60 O atoms. For $SrCO_3(111)$, the model has 20 Sr atoms, 20 C atoms and 60 O atoms.

Results and discussion

Structural features and properties

The experimentally determined Au and Ni^{2+} contents (Au_{exp}, Ni^{2+}_{exp}) agreed with the theoretical values (Au_{theo}, Ni^{2+}_{theo}) based on the ICP-OES results (within an acceptable relative error range of ±10%), providing evidence about the efficiency of the impregnation and photodeposition processes (ESI,† Table S1).

The reflections of cubic $SrTiO_3$ (ICDD 00-035-0734) and orthorhombic $SrCO_3$ (ICDD 01-084-1778) phases were revealed in all XRD patterns of the STO-SCO (HT)-based samples (Fig. 1). No additional reflections were identified in the case of the NiO/STO-SCO (HT) sample (*vs.* STO-SCO (HT)) given by the relatively low loading of NiO on the support.[39,40] According to Sreethawong *et al.*, the characteristic diffraction peak of NiO (at $2\theta = 43.3°$) can be observed for loadings higher than 5 wt%.[39] Although no typical diffraction peaks of Au species (metal Au or Au_xO) were expected in the recorded XRD patterns at such a low Au loading,[41,42] an additional relatively broad reflection can be observed at 38.2° (2θ) in the case of Au-STO-SCO (HT) and Au-NiO/STO-SCO (HT), which corresponds to the (111) plane of the face centered cubic Au-structure.[43,44] Moreover, Rietveld analysis ($SrCO_3$ content determination) and primary crystallite size (PCS) calculation of $SrTiO_3$ (*via* the Scherrer equation) were performed based on the XRD results.
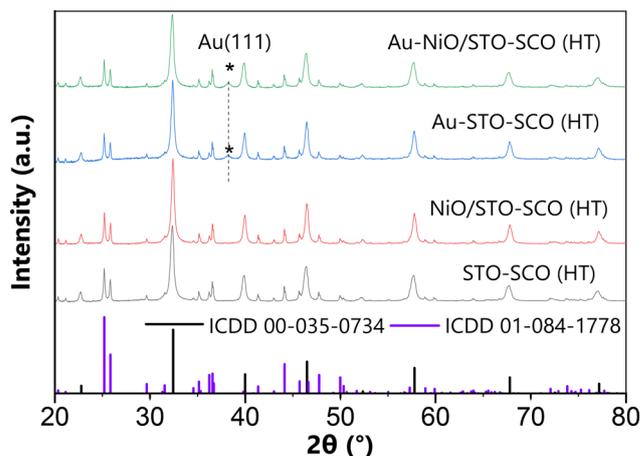

Fig. 1 The XRD patterns of the studied STO-SCO (HT)-based samples.

3462 | *Catal. Sci. Technol.*, 2024, **14**, 3459–3472

This journal is © The Royal Society of Chemistry 2024

Thermal annealing at 700 °C contributed to an increase of the PCS of SrTiO$_3$ (from 19 to 23 nm in the case of the hydrothermally synthesized support, and from 28 to 32 nm in the case of the STO). (Table 1). Similar PCSs were previously observed for SrTiO$_3$ from the hydrothermal process[45] (19.3 nm) and from that after thermal annealing at 700 °C[46] (23 nm).

According to Rietveld analysis, the SCO content of the STO-SCO (HT)-based samples was 18 wt%, which was in accordance with the carbonate-content calculated based on the carbon content of the samples (EA, ~18 wt%), indicating the crystallinity of SCO. Further XRD patterns of the studied samples are presented in the ESI† (Fig. S1–S3, respectively).

The Au-STO-SCO (HT) and Au-NiO/STO-SCO (HT) samples were analyzed *via* XPS. Based on the Ni 2p XP spectrum it can be concluded that mainly Ni^{2+} species[47] (binding energy of 855.56 eV) could be identified, a small fraction of Ni^{3+} species[48] might also be present (with a binding energy of 857.90 eV), and Ni^0 was not formed (ESI,† Fig. S4). Furthermore, the Au 4f XP spectra confirmed the presence of metallic Au (Fig. S5a and b†). No considerable difference was observed in the binding energy values characterizing the electronic state of SrTiO$_3$ (ESI,† Table S2). Furthermore, the experimental (*i.e.*, XPS-based) and theoretical compositions of the species in the case of Au-STO-SCO (HT) and Au-NiO/STO-SCO (HT) were compared (ESI,† Tables S3 and S4).

The morphological features of the studied samples were investigated by SEM and STEM. SEM images of the selected (optimized) samples are presented in Fig. 2. Further SEM images are presented the in ESI† (Fig. S6–S12). Two morphological entities can be revealed in the case of STO-SCO (HT)-based catalysts (Fig. 2), namely nanocubes (STO) and isolated microrods (SCO). While the STO nanocubes have average particle sizes of 20–30 nm, the SCO microrods were 1.0–1.5 μm in length with a diameter of *ca.* 150 nm. The SEM-derived particle size of SrTiO$_3$ agrees with the primary crystallite size from the XRD, calculated *via* the Scherrer equation. While the presence of Au nanospheres was revealed on the SEM images of Au-STO-SCO (HT) and Au-NiO/STO-SCO (HT) (Fig. 2b and c), the morphology of NiO could not be identified at such magnifications, therefore further analyses were performed. The EDX of Au-NiO/STO-SCO (HT) (Fig. 2e) indicated both Au and Ni on the catalyst surface in the case of Au-NiO/STO-SCO (HT). Furthermore, the EDX from SEM of Au-NiO/STO-SCO (HT) (Fig. 2e) showed the

presence of potassium on the surface, which was not entirely removed during the washing step.

To have a closer look on the morphology and the contact between the components, STEM images, EDXS elemental maps and EDX spectra were recorded for the ternary composite, Au-NiO/STO-SCO (HT). As can be seen in the STEM images (Fig. S13†), especially in the medium resolution HAADF image, the support shows rather cubic shaped SrTiO$_3$ particles which apparently have surface indentation or local pores according to the small darker areas. The high-resolution image then shows the NiO particle attached to such an SrTiO$_3$ support particle. In the corresponding EDX spectrum (Fig. S14†) the cloudy like structure was verified to contain Ni and O, but without assigning a certain possible oxidation state. An EDXS elemental map (Fig. S15†) shows the scarcity of the NiO and the Au particles present in the sample and their lack of common localization. However, it appears locally that there are indications of a varying Sr to Ti ratio in the SrTiO$_3$ support (Fig. S16 and S17†) which might be a minority fraction of non-stoichiometric mixed oxides or TiO$_2$ crystallites. Further images and EDXS data (Fig. S18†) show the striking size differences in the SrTiO$_3$ and SrCO$_3$ parts of the Au-NiO/STO-SCO (HT) catalyst.

For an overview on the textural properties of the selected supports, the specific surface area (BET, SSA), the pore volume (BJH, V_P) and the average pore size (r_P) were assessed and are summarized in Table 1. The characteristics of the type IV isotherm with an H3 hysteresis loop were identified (STO-SCO (HT), NiO/STO-SCO (HT) – Fig. S19;† STO, NiO/STO – Fig. S20†), which are characteristic for micro- and mesoporous materials.[49] The highest SSA can be observed for the STO-SCO (HT) sample, which may provide more CO$_2$ adsorption sites and facilitate the involvement of the adsorbed CO$_2$ in the subsequent surface reactions.[50] As expected, the decrease of SSA was observed after sintering at 700 °C[51] (*i.e.*, from 52 m^2 g^{-1} for STO-SCO (HT) to 16 m^2 g^{-1} for NiO/STO-SCO (HT)), however this decrease was obvious only in the case of the hydrothermally synthesized support.

Considerable overlapping of the N$_2$ isotherms was observed in the case of the reference samples (*i.e.*, STO and NiO/STO, Fig. S20†), which indicates that the textural modification after the thermal treatment (at 700 °C, 4 h) of the previously studied samples may be given by the presence of carbonate (*i.e.*, SrCO$_3$). In addition to this, while the pore volume decreased after impregnation in all cases (Table 1,

Table 1 Selected structural features of selected supports

No.	Sample	PCS (STO)	SSA (m^2 g^{-1})	V_P (cm^3 g^{-1})	r_P (nm)
1	STO-SCO (HT)	19	52	0.180	7.040
2	NiO/STO-SCO (HT)	23	16	0.090	11.540
3	STO	28	15	0.770	13.770
4	NiO/STO	32	15	0.070	10.110
5	SCO	26	2–3	0.007	5.350

Remark: PCS – primary crystallite size, SSA – specific surface area, V_P – pore volume, r_P – pore radius.

This journal is © The Royal Society of Chemistry 2024

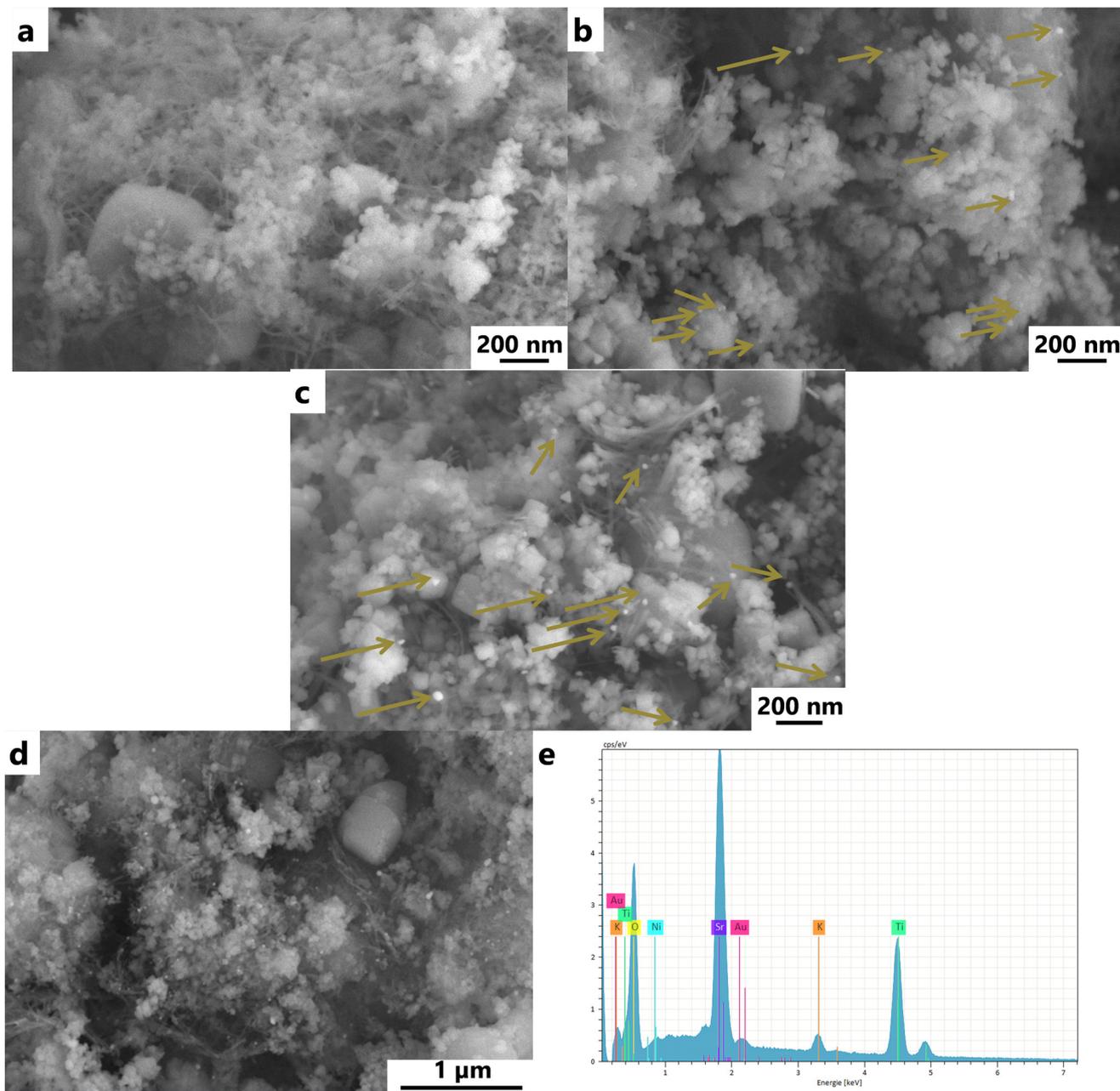*Catal. Sci. Technol.*, 2024, **14**, 3459–3472 | **3463**

Fig. 2 SEM micrograph of (a) NiO/STO-SCO (HT), (b) Au-STO-SCO (HT), (c) and (d) Au-NiO/STO-SCO (HT), (e) EDX of Au-NiO/STO-SCO (HT), presented in d (accelerating voltage: 5 kV in the case of a–c, 10 kV in the case of d, the arrows indicate the Au NPs).

samples no. (1) and (2): from 0.18 to 0.09 cm³ g⁻¹, samples no. (3) and (4): from 0.77 to 0.074 cm³ g⁻¹), unexpectedly the increase of pore size was observed after impregnation and thermal treatment in the case of the carbonate containing support (*i.e.*, STO-SCO (HT): 7.04 nm *vs.* NiO/STO-SCO (HT): 11.54 nm).

Light absorption and electronic structure

To investigate the optical properties of the studied samples, the respective UV-vis diffuse reflectance spectra were recorded (Fig. 4). All the samples possess an absorption edge in the UV region (300–400 nm), highlighted in grey in Fig. 3. Considering the Tauc-plot (Fig. 3, inset) in the case of indirect semiconductors, the band gap energy (ΔE_g) of SrTiO₃ was determined to be 3.2 eV. The determination of the ΔE_g of SrCO₃ was not possible, since it cannot be resolved in the recorded range (200–800 nm).[23] Moreover, considering the overlapping of the absorption edges in the recorded UV region (200–400 nm) and the low NiO loading, the determination of the NiO ΔE_g is not possible based on the recorded spectra of the studied multicomponent systems (*i.e.*, NiO/STO-SCO (HT), Au-NiO/STO-SCO (HT)). However, based on the published literature, it is known that the ΔE_g of
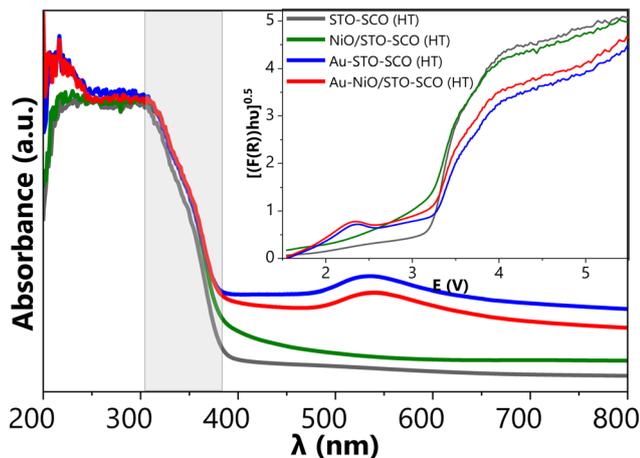
3464 | *Catal. Sci. Technol.*, 2024, **14**, 3459–3472

This journal is © The Royal Society of Chemistry 2024

Fig. 3 The UV–vis spectra of the studied samples in association with their Tauc-plot (inset).
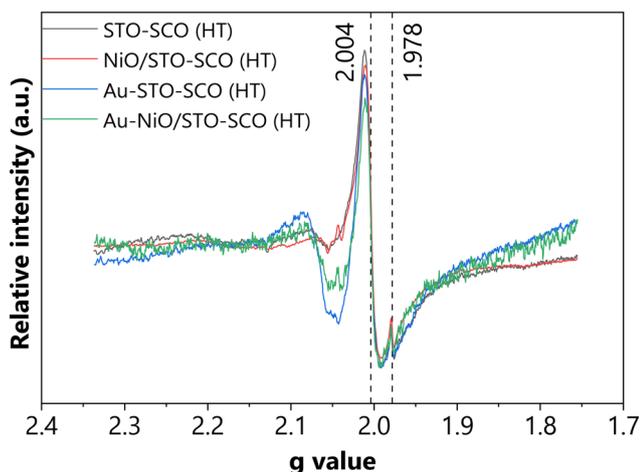

Fig. 4 Representative EPR spectra of the studied catalysts.

NiO is situated in the range of 3.4–4.6 eV.[52,53] In the case of the Au-containing samples (*i.e.*, Au-STO-SCO (HT), Au-NiO/ STO-SCO (HT)), the plasmon resonance band is located at 540 nm, which is directly correlated to the Au NP size and shape.[12,54] Further UV-vis spectra of the reference samples are presented in Fig. S21.†

Unravelling the paramagnetic species under irradiation

To reveal and clarify the presence of paramagnetic species under irradiation, serial recordings were performed under irradiation (ESI,† Fig. S22). The representative extracted EPR spectra of selected catalysts are presented in Fig. 4. Interestingly, in all studied samples a nearly isotropic signal was identified at $g = 2.004$ ($g_1 = g_2 = g_3$), which was assigned to the trapped electrons in oxygen vacancies (OVs)[29,41,55,56] as depicted in Fig. 4 (ESI,† Table S5). Although the presence of OVs was mainly expected after sintering (*i.e.*, in the case of NiO/STO-SCO (HT) and Au-NiO/STO-SCO (HT)) and also after Au photodeposition on the STO-SCO (HT) support (*i.e.*, in the

case of Au-STO-SCO (HT)),[12] their presence was also unexpectedly identified in the case of the bare hydrothermally synthesized support (*i.e.*, STO-SCO (HT)). On the other hand, a relatively weak anisotropic signal was identified at 1.978, which may be assigned to the Ti^{3+} centers (ESI,† Table S5).[55,57] In the case of the Au-containing samples (*i.e.*, Au-STO-SCO (HT) and Au-NiO/STO-SCO (HT)), a relatively broad signal can be observed at $g = 2.066$, which can be correlated to the interaction between Au nanoparticles and OVs from $SrTiO_3$.[55,58]

In situ DRIFTS

The formation of surface species after the exposure of the tested (selected) photocatalysts to CO_2, and the influence of light irradiation on the CO_2 adsorption, were studied using *in situ* DRIFTS, and the results are presented in Fig. 5 and S23–S28.† Recently, the adsorption mechanisms over metal oxides under irradiation have been studied *via in situ* DRIFTS.[59,60] The spectral differences during CO_2 adsorption in the dark *vs.* under irradiation may be caused by the: (1) light induced oxygen desorption and implicitly increased amount of Lewis acid sites,[61] (2) different activation of adsorbed CO_2, (3) different interaction of CO_2 with pre-adsorbed hydroxyl groups, (4) enhanced splitting of hydroxyl groups and transfer of hydrogen to adsorbed CO_2.[62]
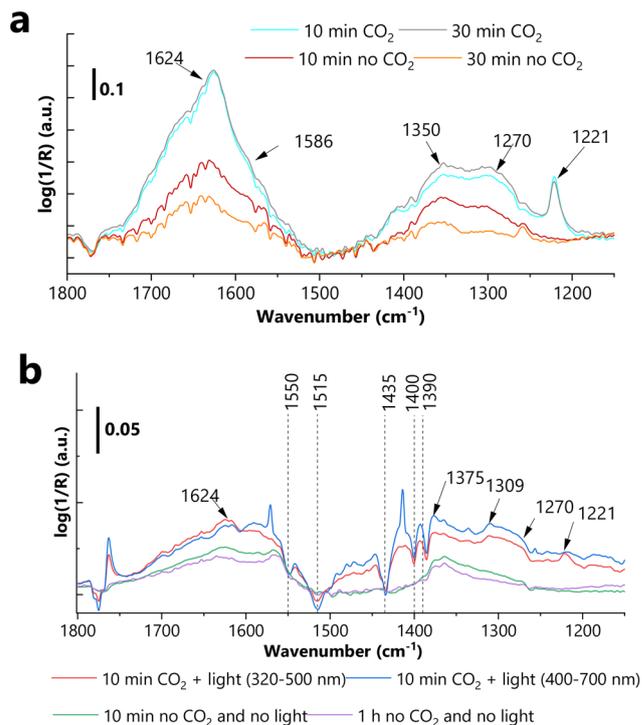

Fig. 5 (a) DRIFT spectra of Au-NiO/STO-SCO (HT) (dark). (b) DRIFT spectra of Au-NiO/STO-SCO (HT) under irradiation (remark: the consecutive negative and positive peaks (in the region of 1775–1750 cm^{-1}) are a result of shift of signals, which are already present in the background).

This journal is © The Royal Society of Chemistry 2024

Catal. Sci. Technol., 2024, **14**, 3459–3472 | **3465**

Since our primary intention was to unravel the visible light-induced (*i.e.*, 500–700 nm) transformations (thus assessing the involvement of the SPR effect of Au NPs), a comparative analysis was performed (and presented in the ESI† – *i.e.*, Tables S6–S9) based on the spectra recorded in the dark *vs.* under irradiation ((i) 320–400 nm or (ii) 500–700 nm).

Apart from the appearance of certain negative features (due to the spectator species, detailed discussion presented in the ESI†) under light irradiation *vs.* in the dark in the case of STO-SCO (HT), NiO/STO-SCO (HT) and Au-STO-SCO (HT) samples, no considerable differences were observed. For this reason, only the representative DRIFT spectra will be presented in the next section (*i.e.*, for Au-NiO/STO-SCO (HT), Fig. 5), in addition to commenting on the influence of light on CO_2 adsorption for all studied catalysts.

Under irradiation negative bands were identified at 1435, 1400 and 1390 cm^{-1} for all examined samples (Fig. S24, S26 and S28†), which can be directly assigned to the structural carbonates or spectator carbonate species present in the beginning of the measurement. Moreover, the Au-NiO/STO-SCO (HT) sample exhibited two additional negative features, at 1550 and 1515 cm^{-1} (Fig. 5). These structural carbonates or spectator carbonate species can participate in the formation of (presumably) structurally very different species. These newly formed species can be identified only in the presence of CO_2, and they completely disappear when CO_2 is removed. The potential assignment of the previously mentioned features is the following: $v_{as}(OCO)$ at 1550 cm^{-1},[63] $v_s(OCO)$ at 1390 and 1435 cm^{-1} (ref. 63–68) from bicarbonate species, respectively, $v_{as}(OCO)$ at 1515 cm^{-1},[69] $v_s(CO_3)$ at 1435,[63] and $v_s(OCO)$ at 1400 cm^{-1} (ref. 69) from monodentate carbonate.

It should be highlighted that under visible light irradiation (500–700 nm) the only observable signals can be identified at 1414 and 1560 cm^{-1} in Table S6.† These can be associated with the characteristic vibrational modes, *i.e.*, $v_{as}(COH)$ at 1414 cm^{-1} (ref. 70 and 71) and $v_{as}(OCO)$[69] at 1560 cm^{-1},[72] of bidentate bicarbonates. Furthermore, the previously formed bicarbonates (*i.e.*, at 1221 and 1624 cm^{-1}, under λ = 320–400 nm) cannot be identified in the spectra

recorded under λ = 500–700 nm, which indicates their visible light-induced transformation (ESI,† Fig. S24, S26 and S28).

From the spectra presented in Fig. S23–S28,† it can be concluded that no considerable differences were observed for all four studied photocatalysts (Au-NiO/STO-SCO (HT), Au-STO-SCO (HT), NiO/STO-SCO (HT) and STO-SCO (HT)) under dark conditions. In other words, the presence of ~0.3 wt% NiO and ~1 wt% Au has negligible effect on CO_2 adsorption in the dark. In the studied spectra the observed species were identified to be linearly adsorbed CO_2, monodentate carbonate, monodentate bicarbonates and carboxylates. In addition to the previously identified species, bidentate carbonate was identified in the spectra of Au-STO-SCO (HT). Under (visible or UV-A) light irradiation though, remarkable differences were identified. One considerable difference is related to the visible-light induced transformation of monodentate bicarbonates over Au-NiO/STO-SCO (HT). Finally, regardless of the thermal treatment performed before CO_2 adsorption (described in the Experimental section), the vibration feature corresponding to the COH bending (at 1222 cm^{-1}) was always observed, which is a clear indication of the presence of hydroxyl groups on the surface for all studied samples.

Photocatalytic CO_2 reduction

The products formed and their normalized concentrations (in ppm g_{cat}^{-1} h^{-1}) from the photoreduction of CO_2 using $SrTiO_3$-based catalysts under Hg–Xe light irradiation are presented in Fig. 6 (ESI,† raw data: Fig. S29–S36). Beyond the presented results, additional samples were analyzed, namely STO-SCO (SM), SCO and Au-SCO. No product formation was observed in the case of SCO and Au-SCO. The activity of STO-SCO (SM) was 17 ppm g_{cat}^{-1} h^{-1} towards CH_4 generation. Investigations of the long-term reusability and photocatalytic stability of the tested catalysts were not performed, as this work focuses on the influence of catalyst composition and the interaction between the individual sub-components, on product formation and selectivity (Fig. 6).

Considerably higher activity and selectivity were observed in the case of STO-SCO (HT)-supported *vs.* STO-supported
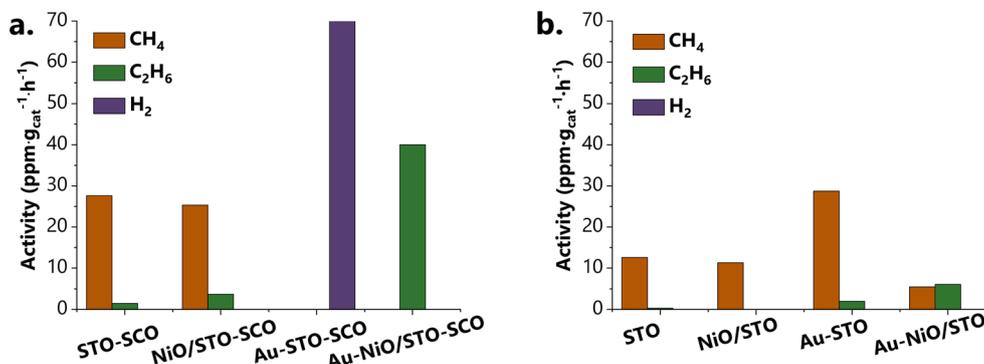

Fig. 6 a. The activity of the STO-SCO (HT)-based samples. b. The activity of the reference series of the samples (*i.e.*, STO-based samples).

3466 | *Catal. Sci. Technol.*, 2024, **14**, 3459–3472

This journal is © The Royal Society of Chemistry 2024

samples. To understand the differences in activity in the case of STO- and STO-SCO-based samples, the charge transfer mechanism was studied. Conduction (CB) and valence band (VB) edges of the single components (SrTiO$_3$, SrCO$_3$, and NiO) were calculated using experimental results (Mott–Schottky plot, band gaps) and literature reported data (see ESI,† Fig. S37 and S38). Results show that the CB edge minimum of NiO (−3.03 V vs. NHE) is more negative than that of STO (CB: −1.00 V vs. NHE) and SCO (−0.64 V vs. NHE). Otherwise, the VB edge maximum of SCO (4.30 V vs. NHE) is more positive than that of STO (2.10 V vs. NHE) and NiO (0.37 V vs. NHE). Additionally, the electronic properties of SrTiO$_3$ and SrCO$_3$ were calculated using DFT. The main aspects related to the calculations will be presented shortly in the next section.

(1) Influence of SrCO$_3$. Currently, the role of SrCO$_3$ in SrTO$_3$-SrCO$_3$ systems is still a matter of debate. Although most of the studies assigns SrCO$_3$ as a co-catalyst,[73] different approaches are presented in the literature related to the charge transfer in SrTiO$_3$-SrCO$_3$ systems, which either neglects (1.1)[20,21] or accounts for (1.2, Fig. 7) the formation of the internal electric field at the contact between SrTiO$_3$ and SrCO$_3$.[74]

(1.1) Several scientific studies (Li and coworkers[20] and Jin and coworkers[21]) report that the efficient charge separation is given by the functionality of SrCO$_3$ as an electron trap (Fig. S39†). This approach assumes the accumulation of electrons in the CB of SrCO$_3$, and the localization of holes at the VB of SrTiO$_3$. However, based on this charge transfer scheme, it is highly possible that CO$_2$ reduction would take place over SrCO$_3$. At the same time, it must be highlighted that this approach does not account for the band bending and the

formation of an electric field. One can explain the validity of this approach by the fact that since SrCO$_3$ is an insulator, no charge transfer would take place (given by the large work function difference between SrTiO$_3$ and SrCO$_3$), and subsequently, there would be no band bending or generation of an interfacial electric field.

(1.2) With the building of a semiconductor–insulator (SrTiO$_3$-SrCO$_3$) heterojunction a Fermi level alignment between SrTiO$_3$ and SrCO$_3$ might occur resulting in the formation of a built-in electric field which points from SrTiO$_3$ to SrCO$_3$ as suggested by Han[74] (Fig. 7). Considering the direction of the built-in electric field, the transfer of the electrons from the CB of SrTiO$_3$ to the CB of SrCO$_3$ is not possible. However, during the heterojunction formation, generation of OVs and surface doping of SrCO$_3$ might occur leading to the formation of an intermediate electronic level (IL) over the SrCO$_3$ near the interphase for which $|E_{VB} - E_{IL}|$ = $\Delta E_{(VB–IL)} \leq h\nu$. At such circumstance, under irradiation a translocation of electrons from the VB of SrCO$_3$ to its IL and from there to the CB of SrCO$_3$ would be possible. Electrons from the IL of SrCO$_3$ might also be transferred to the VB of SrTiO$_3$, where they can recombine with holes from the VB of SrTiO$_3$ which will suppress the charge carrier recombination between $h^+_{VB,SrTiO_3}$ and $e^-_{CB,SrTiO_3}$.

To investigate the possibility of a built-in electric field formation in the case of SrTiO$_3$-SrCO$_3$ (which would be the result of the Fermi level alignment after contact between SrTiO$_3$ and SrCO$_3$, as depicted in Fig. 7) the work function (and implicitly the Fermi level) of the pure (i.e., SrTiO$_3$, SrCO$_3$) and doped materials (C-doped SrTiO$_3$, Ti-doped SrCO$_3$) was calculated via computational methods. As already described in the Methods section, the SrTiO$_3$(110) and
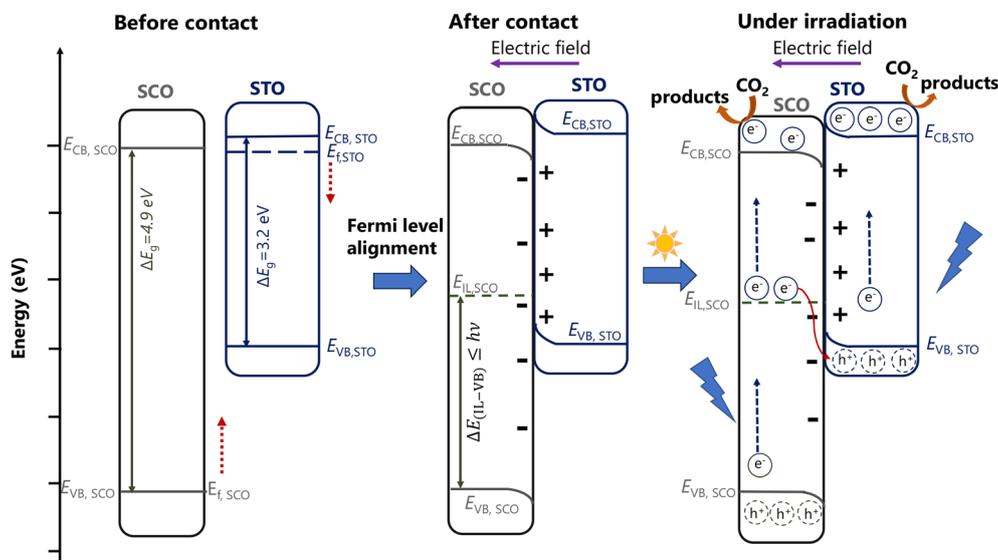

Fig. 7 Scheme of the charge transfer in the case of SrTiO$_3$-SrCO$_3$ via accounting the formation of the internal electric field – rebuilt based on the work written by Han and coworkers[74] (CB – conduction band, IL – intermediate level, SCO – SrCO$_3$, STO – SrTiO$_3$, VB – valence band); remarks: (i) – the conduction and valence band positions of STO and SCO were taken from the literature[20,21] and (ii) the red arrows in the left side ("before contact") indicate the Fermi level alignment of each component.

This journal is © The Royal Society of Chemistry 2024

Catal. Sci. Technol., 2024, **14**, 3459–3472 | 3467

SrCO$_3$(111) slab models were built. As to SrTiO$_3$(110), two different terminations (SrO- and TiO-) were considered. To study the interaction between SrTiO$_3$(110) and SrCO$_3$(111), both terminations of SrTiO$_3$(110) were doped by a C atom, *i.e.*, one surface Ti atom was replaced by a C atom. As to SrCO$_3$(111), one surface C atom was replaced by a Ti atom. Then, the density of states of all the surfaces was calculated. Furthermore, the work function (Φ) was calculated based on $\Phi = E_{vac} - E_f$ (E_{vac} is the vacuum potential and E_f is the Fermi energy). The models and density of states are shown in the ESI† (Fig. S42–S46) and the work functions are listed in Table 2. Based on the computational results listed in Table 2, the termination of SrTiO$_3$ (either SrO- or TiO-terminated, cases 1.1 and 1.2) influences significantly the absolute value of the work function (*i.e.*, 5.7 *vs.* 2.1 eV). Similar observations were reported by Jacobs and coworkers[75] based on their computational investigations. Most studies in the literature consider the electronic properties of TiO-terminated SrTiO$_3$(110), which define a difference of work function of 3.6 eV (and implicitly a difference in the Fermi level) between SrTiO$_3$ and SrCO$_3$. This also implies that the termination of SrTiO$_3$ (SrO- and TiO-termination) in contact with SrCO$_3$ is a decisive factor. The computational results support the hypotheses related to the direction of the Fermi level shift (Table 2) after the interaction between the two components (as marked in Fig. 7). While the work function increases in the case of C-doped SrTiO$_3$(110) (for both terminations), the work function of Ti-doped SrCO$_3$(111) decreases. The Fermi level shift in both components leads to the generation of an internal electric field, which agrees with the results presented by Han and coworkers.[74] The computational results are presented in detail in the ESI† (Fig. S42–S46).

The methane formation rate during batch cleaning (gas mixture: He + H$_2$O) over STO-SCO (HT) catalysts was higher when compared to that of STO (Fig. S29 and S33†) which indicates the participation of SrCO$_3$ in CH$_4$ formation. Here, CH$_4$ might be formed by the reaction of adsorbed carbon species and photogenerated charge carriers. Because no methane formation was observed when using SCO, it is assumed that the higher activity of STO-SCO (HT) compared to STO is mainly caused by a larger number of photocatalytic active species. However, the direct participation of the SrCO$_3$ phase in product formation over STO-SCO (HT) cannot be excluded completely. To exclude the influence of the structural peculiarities of SrCO$_3$ and SrTiO$_3$ when it comes to the hydrothermally synthesized and commercially available samples (different morphology), the activity of STO and of STO-SCO (SM) in CO$_2$ reduction was also compared (*i.e.*, 12

vs. 17 ppm g$_{cat}^{-1}$ h^{-1} STO *vs.* STO-SCO (SM)). Again, the presence of SCO (in STO-SCO (SM)) leads to higher activity.

(2) Influence of NiO. The charge transfer mechanism (mainly for photocatalytic H$_2$O splitting) has already been reported for NiO/SrTiO$_3$[76,77] and NiO/TiO$_2$.[39,40,78,79] When an n-type and a p-type semiconductor are brought into close contact (*i.e.*, SrTiO$_3$ and NiO), the Fermi level alignment, the establishment of an interfacial built-in electric field, the interfacial band bending and the charge transfer must all be considered[80] (Fig. S40†). Under irradiation the e$^-$ from the VB of both photoactive components will transfer into their CB leaving behind positive charged holes (h$^+$). Assuming that NiO is mainly formed on the surface of SrTiO$_3$, and considering the built-in electric field (with a direction from SrTiO$_3$ to NiO), the e$^-$ from the CB of NiO is transferred to the CB of STO (*i.e.*, the electron transfer in the opposite direction of the built-in electric field)[80] (Fig. S40†), and CO$_2$ reduction takes place over SrTiO$_3$. So, NiO acts as an electron donor in NiO/STO. The functionality of NiO remains the same in the case of NiO/STO-SCO (HT) systems (considering the alignment of Fermi levels) as long as Φ(STO-SCO(HT)) < Φ(NiO). However, because of the low NiO content in the composite (Table S1†), the overall effect of NiO on CO$_2$ reduction was expected to be relatively low (Fig. 7: STO *vs.* NiO/STO, STO-SCO (HT) *vs.* NiO/STO-SCO (HT)).

(3) Influence of Au. Analyzing the hypothetical charge transfer mechanism in Au-SrTiO$_3$ (general mechanism in the case of an n-type semiconductor and Au reported in the literature,[17] Fig. S41†), electrons are injected from Au to the CB of SrTiO$_3$, and CO$_2$ reduction occurs over SrTiO$_3$. However, if SrCO$_3$ is present, the Fermi level alignment between SrTiO$_3$ and SrCO$_3$ takes place prior to the contact with Au. According to the aligned Fermi level between SrTiO$_3$ and SrCO$_3$, different mechanisms are probable. If $E_{f,aligned}$ (SrTiO$_3$-SrCO$_3$) < E_f(Au), the internal electric field will point from the metal (Au) to SrTiO$_3$-SrCO$_3$, which guides the electrons from the support to Au.[17] In the contrary case ($E_{f,aligned}$ (SrTiO$_3$-SrCO$_3$) > E_f(Au)), a charge carrier transport similar to that depicted in Fig. S41† occurs.

Enhanced CH$_4$ production was observed over Au-STO *vs.* STO samples (Fig. 6b), which can be correlated with the involvement of Au NPs as an electron donor.[15] In contrast to this, over Au-STO-SCO (HT) the formation of carbon-based products in the presence of CO$_2$ was similar to that for batch cleaning and H$_2$ was the main product in CO$_2$ reduction over this catalyst. Hydrogen generation over Au during photocatalytic CO$_2$ reduction was already reported by Pougin *et al.* using Au@TiO$_2$ catalysts.[81] Hydrogen formation is both

Table 2 Calculated work function of different surfaces

Case	Surface	Φ (eV)	Modified surface	Φ (eV)	$\Delta\Phi$ (eV)
1. SrTiO$_3$	1.1. SrO-terminated SrTiO$_3$(110)	5.7	C-doped SrO-terminated SrTiO$_3$(110)	6.1	0.4
	1.2. TiO-terminated SrTiO$_3$(110)	2.1	C-doped TiO-terminated SrTiO$_3$(110)	2.3	0.2
2. SrCO$_3$	SrCO$_3$(111)	5.7	Ti-doped SrCO$_3$(111)	5.3	−0.4

kinetically and thermodynamically a more facile reaction (*vs.* CO_2-to-CH_4 or CO_2-to-CO).[82–84] One reason for the various reaction products obtained over Au-STO and Au-STO-SCO (HT) might be the differences between the Fermi level of the corresponding support and the Fermi level of Au. For Au-STO-SCO (HT), the Fermi level of the support is assumed to be lower than that of Au ($E_{f,aligned}$ ($SrTiO_3$-$SrCO_3$) < E_f(Au). After alignment, electrons from the STO-SCO (HT) support will be transferred to Au where H_2 formation will occur under irradiation, In addition to this, $SrCO_3$ may contribute to the spatial isolation of the sites for H^+ and electrons in the presence of CO_2 and H_2O[41,84] in the case of Au-STO-SCO (HT) *vs.* (Au-STO), which leads to the formation of H_2. For Au-STO, the electron transfer is expected in the opposite direction as shown in Fig. S41.† The transferred electrons react on the $SrTiO_3$ surface with activated CO_2 and protons to form mainly CH_4.

(4) Mutual effect of Au and NiO in STO-based systems. STEM (ESI,† Fig. S13) and SEM (Fig. 2 and S10†) results give no hints of Au–Ni alloy formation. According to Fig. 6b, CO_2 reduction over Au-NiO/STO takes place with lower rates as in the case of Au-STO. Interestingly, already the presence of both NiO and Au on STO alone improves C_2H_6 formation slightly compared to the pure support. However, over Au-NiO/STO-SCO (HT) (Fig. 6a) C_2H_6 was observed as the single product with relatively high formation rate. Formation of C2 products from CO_2 followed a complex reaction pathway whose key step is the C–C coupling.[85] It seems that the simultaneous presence of Au and NiO supports such coupling processes which occur in monometallic catalysts only to a minor extent. The role of the single compound in the C2 formation process is still unclear. One reason for the high C_2H_6 selectivity might be an increased local temperature of the Au-NiO/STO-SCO (HT) surface (given by the simultaneous presence of a Schottky junction and OVs, as suggested by Cai and coworkers[41]) which facilitates the mobility of the intermediates formed as well as the desorption of the C2 products from the surface of the photocatalyst.[41] Thereby, NiO might play a role in the activation of CO_2.[62]

Conclusions

In summary, the individual and simultaneous influence of $SrCO_3$, NiO and Au on the photocatalytic CO_2 reduction activity of $SrTiO_3$-based materials was studied. Based on experimental and computational investigations the following conclusions can be drawn:

• The presence of $SrCO_3$ has a positive effect on the photocatalytic activity of $SrTiO_3$ in CO_2 reduction. It is assumed that by using a $SrTiO_3$-$SrCO_3$ heterojunction a higher number of reactive species are available for the reaction under irradiation compared to pure $SrTiO_3$.

• The low amount of NiO (0.3 wt%) (on either supports: $SrTiO_3$, $SrTiO_3$-$SrCO_3$) has only a minor effect on the activity and product formation.

• CO_2 reduction products of Au containing samples are affected by the support. In the case of Au-$SrTiO_3$ mainly CH_4 was formed, whereas for Au-$SrTiO_3$-$SrCO_3$ H_2 was the main product. This difference in product formation might be explained by considering Fermi level alignment.

• The simultaneous presence of Au and NiO on the $SrTiO_3$-$SrCO_3$ surface supports the dimerization of C1 intermediates.

Conflicts of interest

There are no conflicts to declare.

Acknowledgements

References

1 NASA, *Global Climate Change*, **https://climate.nasa.gov/vital-signs/carbon-dioxide/** (last accessed on 05.02.2024).

2 *World Energy Outlook 2022*, 2022, pp. 233–236, **https://iea.blob.core.windows.net/assets/7e42db90-d8ea-459d-be1e-1256acd11330/WorldEnergyOutlook2022.pdf.**

3 Y.-F. Xu, M. Lee, Y. Jun and G. A. Ozin, Perovskite, the chameleon CO_2 photocatalyst, *Cell Rep. Phys. Sci.*, 2021, **2**(1), 100300.

4 C. Luo, J. Zhao, Y. Li, W. Zhao, Y. Zeng and C. Wang, Photocatalytic CO_2 reduction over $SrTiO_3$: Correlation between surface structure and activity, *Appl. Surf. Sci.*, 2018, **447**, 627–635.

5 J. Shan, F. Raziq, M. Humayun, W. Zhou, Y. Qu, G. Wang and Y. Li, Improved charge separation and surface activation via boron-doped layered polyhedron $SrTiO_3$ for co-catalyst free photocatalytic CO_2 conversion, *Appl. Catal., B*, 2017, **219**, 10–17.

6 W. He, X. Wu, Y. Li, J. Xiong, Z. Tang, Y. Wei, Z. Zhao, X. Zhang and J. Liu, Z-scheme heterojunction of SnS2-decorated 3DOM-$SrTiO_3$ for selectively photocatalytic CO_2 reduction into CH_4, *Chin. Chem. Lett.*, 2020, **31**(10), 2774–2778.

This journal is © The Royal Society of Chemistry 2024

Catal. Sci. Technol., 2024, **14**, 3459–3472 | **3469**

7 K. Xie, N. Umezawa, N. Zhang, P. Reunchan, Y. Zhang and J. Ye, Self-doped SrTiO$_{3-\delta}$ photocatalyst with enhanced activity for artificial photosynthesis under visible light, *Energy Environ. Sci.*, 2011, **4**(10), 4211–4219.

8 W. Zhao, W. Zhao, G. Zhu, T. Lin, F. Xu and F. Huang, Black strontium titanate nanocrystals of enhanced solar absorption for photocatalysis, *CrystEngComm*, 2015, **17**(39), 7528–7534.

9 H. Tan, Z. Zhao, W.-b. Zhu, E. N. Coker, B. Li, M. Zheng, W. Yu, H. Fan and Z. Sun, Oxygen vacancy enhanced photocatalytic activity of pervoskite SrTiO$_3$, *ACS Appl. Mater. Interfaces*, 2014, **6**(21), 19184–19190.

10 N. G. Moustakas and J. Strunk, Photocatalytic CO$_2$ Reduction on TiO$_2$-Based Materials under Controlled Reaction Conditions: Systematic Insights from a Literature Study, *Chem. – Eur. J.*, 2018, **24**(49), 12739–12746.

11 M. Dilla, A. Pougin and J. Strunk, Evaluation of the plasmonic effect of Au and Ag on Ti-based photocatalysts in the reduction of CO$_2$ to CH$_4$, *J. Energy Chem.*, 2017, **26**(2), 277–283.

12 J. B. Priebe, J. R. Radnik, A. J. Lennox, M.-M. Pohl, M. Karnahl, D. Hollmann, K. Grabow, U. Bentrup, H. Junge and M. Beller, Solar hydrogen production by plasmonic Au–TiO$_2$ catalysts: impact of synthesis protocol and TiO$_2$ phase on charge transfer efficiency and H$_2$ evolution rates, *ACS Catal.*, 2015, **5**(4), 2137–2148.

13 C. Wang, O. Ranasingha, S. Natesakhawat, P. R. Ohodnicki, M. Andio, J. P. Lewis and C. Matranga, Visible light plasmonic heating of Au–ZnO for the catalytic reduction of CO$_2$, *Nanoscale*, 2013, **5**(15), 6968–6974.

14 L. Liu, P. Li, B. Adisak, S. Ouyang, N. Umezawa, J. Ye, R. Kodiyath, T. Tanabe, G. V. Ramesh and S. Ueda, Gold photosensitized SrTiO$_3$ for visible-light water oxidation induced by Au interband transitions, *J. Mater. Chem. A*, 2014, **2**(25), 9875–9882.

15 Y. Ham, T. Minegishi, T. Hisatomi and K. Domen, A SrTiO$_3$ photoanode prepared by the particle transfer method for oxygen evolution from water with high quantum efficiencies, *Chem. Commun.*, 2016, **52**(28), 5011–5014.

16 F. Horikiri, T. Ichikawa, K. Sato, K. Yashiro, T. Kawada and J. Mizusaki, The Barrier Formation Mechanism on SrTiO$_3$ for High-Temperature Photo-Electronic Devices, *ECS Trans.*, 2009, **16**(51), 451.

17 W. Guo, J. Huang and W. D. Wei, Plasmonic Metal/Semiconductor Heterostructures, in *Plasmonic Catalysis: From Fundamentals to Applications*, ed. P. H. C. Camargo and E. Cortés, Wiley-VCH, Weinheim, Germany, 2021, pp. 295–322.

18 K. Shao, Y. Wang, M. Iqbal, L. Lin, K. Wang, X. Zhang, M. He and T. He, Modification of Ag nanoparticles on the surface of SrTiO$_3$ particles and resultant influence on photoreduction of CO$_2$, *Appl. Surf. Sci.*, 2018, **434**, 717–724.

19 L. Collado, A. Reynal, F. Fresno, M. Barawi, C. Escudero, V. Perez-Dieste, J. M. Coronado, D. P. Serrano, J. R. Durrant and V. A. de la Peña O'Shea, Unravelling the effect of charge dynamics at the plasmonic metal/semiconductor interface for CO$_2$ photoreduction, *Nat. Commun.*, 2018, **9**(1), 4986.

20 Z. Li, P. Zheng, W. Zhang, S. Gong, L. Zhu, J. Xu, F. Rao, X. Xie and G. Zhu, Constructing SrCO$_3$/SrTiO$_3$ nanocomposites with highly selective photocatalytic CO$_2$-to-CO reduction, *Colloids Surf., A*, 2022, 129686.

21 S. Jin, G. Dong, J. Luo, F. Ma and C. Wang, Improved photocatalytic NO removal activity of SrTiO$_3$ by using SrCO$_3$ as a new co-catalyst, *Appl. Catal., B*, 2018, **227**, 24–34.

22 X. Pan, X. Chen and Z. Yi, Photocatalytic oxidation of methane over SrCO$_3$ decorated SrTiO$_3$ nanocatalysts via a synergistic effect, *Phys. Chem. Chem. Phys.*, 2016, **18**(46), 31400–31409.

23 B. Boga, N. Steinfeldt, N. G. Moustakas, T. Peppel, H. Lund, J. Rabeah, Z. Pap, V.-M. Cristea and J. Strunk, Role of SrCO$_3$ on Photocatalytic Performance of SrTiO$_3$-SrCO$_3$ Composites, *Catalysts*, 2022, **12**(9), 978.

24 A. Pougin, M. Dilla and J. Strunk, Identification and exclusion of intermediates of photocatalytic CO$_2$ reduction on TiO$_2$ under conditions of highest purity, *Phys. Chem. Chem. Phys.*, 2016, **18**(16), 10809–10817.

25 C. Xin, M. Hu, K. Wang and X. Wang, Significant enhancement of photocatalytic reduction of CO$_2$ with H$_2$O over ZnO by the formation of basic zinc carbonate, *Langmuir*, 2017, **33**(27), 6667–6676.

26 T. Mahmood, M. T. Saddique, A. Naeem, P. Westerhoff, S. Mustafa and A. Alum, Comparison of different methods for the point of zero charge determination of NiO, *Ind. Eng. Chem. Res.*, 2011, **50**(17), 10017–10023.

27 K. Domen, S. Naito, T. Onishi, K. Tamaru and M. Soma, Study of the photocatalytic decomposition of water vapor over a nickel (II) oxide-strontium titanate (SrTiO$_3$) catalyst, *J. Phys. Chem.*, 1982, **86**(18), 3657–3661.

28 J. F. Fernando, M. P. Shortell, C. J. Noble, J. R. Harmer, E. A. Jaatinen and E. R. Waclawik, Controlling Au photodeposition on large ZnO nanoparticles, *ACS Appl. Mater. Interfaces*, 2016, **8**(22), 14271–14283.

29 S. Han, L. Yu, H. Zhang, Z. Chu, X. Chen, H. Xi and J. Long, Gold plasmon-enhanced solar hydrogen production over SrTiO$_3$/TiO$_2$ heterostructures, *ChemCatChem*, 2019, **11**(24), 6203–6207.

30 A. Monshi, M. R. Foroughi and M. R. Monshi, Modified Scherrer equation to estimate more accurately nano-crystallite size using XRD, *World J. Nano Sci. Eng.*, 2012, **2**(3), 154–160.

31 N. G. Moustakas, M. Klahn, B. T. Mei, A. Pougin, M. Dilla, T. Peppel, S. Ristig and J. Strunk, A high-purity gas-solid photoreactor for reliable and reproducible photocatalytic CO$_2$ reduction measurements, *HardwareX*, 2023, e00448.

32 DIN SPEC 91457 Photocatalysis - Determination of product formation in CO$_2$ reduction, **https://www.din.de/en/wdc-beuth:din21:370373675** (last accessed on 14.12.2023).

33 G. Kresse and J. Hafner, First-principles study of the adsorption of atomic H on Ni (111), (100) and (110), *Surf. Sci.*, 2000, **459**(3), 287–302.

34 G. Kresse and J. Furthmüller, Efficiency of ab-initio total energy calculations for metals and semiconductors using a plane-wave basis set, *Comput. Mater. Sci.*, 1996, **6**(1), 15–50.

3470 | *Catal. Sci. Technol.*, 2024, **14**, 3459–3472

This journal is © The Royal Society of Chemistry 2024

35 G. Kresse and J. Furthmüller, Efficient iterative schemes for ab initio total-energy calculations using a plane-wave basis set, *Phys. Rev. B: Condens. Matter Mater. Phys.*, 1996, **54**(16), 11169–11186.

36 P. E. Blöchl, Projector augmented-wave method, *Phys. Rev. B: Condens. Matter Mater. Phys.*, 1994, **50**(24), 17953–17979.

37 G. Kresse and D. Joubert, From ultrasoft pseudopotentials to the projector augmented-wave method, *Phys. Rev. B: Condens. Matter Mater. Phys.*, 1999, **59**(3), 1758–1775.

38 J. P. Perdew, K. Burke and M. Ernzerhof, Generalized Gradient Approximation Made Simple, *Phys. Rev. Lett.*, 1996, **77**(18), 3865–3868.

39 T. Sreethawong, Y. Suzuki and S. Yoshikawa, Photocatalytic evolution of hydrogen over mesoporous TiO_2 supported NiO photocatalyst prepared by single-step sol–gel process with surfactant template, *Int. J. Hydrogen Energy*, 2005, **30**(10), 1053–1062.

40 R. Vinoth, P. Karthik, K. Devan, B. Neppolian and M. Ashokkumar, TiO_2–NiO p–n nanocomposite with enhanced sonophotocatalytic activity under diffused sunlight, *Ultrason. Sonochem.*, 2017, **35**, 655–663.

41 S. Cai, J. Chen, Q. Li and H. Jia, Enhanced photocatalytic CO_2 reduction with photothermal effect by cooperative effect of oxygen vacancy and Au cocatalyst, *ACS Appl. Mater. Interfaces*, 2021, **13**(12), 14221–14229.

42 A. I. Rabee, D. Zhao, S. Cisneros, C. R. Kreyenschulte, V. Kondratenko, S. Bartling, C. Kubis, E. V. Kondratenko, A. Brückner and J. Rabeah, Role of interfacial oxygen vacancies in low-loaded Au-based catalysts for the low-temperature reverse water gas shift reaction, *Appl. Catal., B*, 2023, **321**, 122083.

43 H. Sun, J. He, J. Wang, S.-Y. Zhang, C. Liu, T. Sritharan, S. Mhaisalkar, M.-Y. Han, D. Wang and H. Chen, Investigating the multiple roles of polyvinylpyrrolidone for a general methodology of oxide encapsulation, *J. Am. Chem. Soc.*, 2013, **135**(24), 9099–9110.

44 B.-Y. Wang, Y.-S. Hsiao, P.-C. Wei, Y.-T. Liu, C.-C. Chu and V. K. Hsiao, Visible Light-Induced Photocatalyst with Au/TiO_2 Nanocomposites Fabricated through Pulsed Laser-Induced Photolysis, *Catalysts*, 2022, **12**(5), 564.

45 M. Yadav, T. Gyulavári, J. Kiss, K. B. Ábrahámné, A. Efremova, Á. Szamosvölgyi, Z. Pap, A. Sápi, Á. Kukovecz and Z. Kónya, Noble metal nanoparticles and nanodiamond modified strontium titanate photocatalysts for room temperature CO production from direct hydrogenation of CO_2, *J. CO2 Util.*, 2023, **78**, 102621.

46 T. Klaytae, P. Panthong and S. Thountom, Preparation of nanocrystalline $SrTiO_3$ powder by sol–gel combustion method, *Ceram. Int.*, 2013, **39**, S405–S408.

47 S. Gerhold, M. Riva, Z. Wang, R. Bliem, M. Wagner, J. Osiecki, K. Schulte, M. Schmid and U. Diebold, Nickel-oxide-modified $SrTiO_3$ (110)-(4× 1) surfaces and their interaction with water, *J. Phys. Chem. C*, 2015, **119**(35), 20481–20487.

48 Y. Chen, J. Kang, B. Chen, B. Gao, L. Liu, X. Liu, Y. Wang, L. Wu, H. Yu and J. Wang, Microscopic mechanism for

49 unipolar resistive switching behaviour of nickel oxides, *J. Phys. D: Appl. Phys.*, 2012, **45**(6), 065303.

49 R. Bardestani, G. S. Patience and S. Kaliaguine, Experimental methods in chemical engineering: specific surface area and pore size distribution measurements—BET, BJH, and DFT, *Can. J. Chem. Eng.*, 2019, **97**(11), 2781–2791.

50 J. Di, C. Chen, C. Zhu, P. Song, J. Xiong, M. Ji, J. Zhou, Q. Fu, M. Xu and W. Hao, Bismuth vacancy-tuned bismuth oxybromide ultrathin nanosheets toward photocatalytic CO_2 reduction, *ACS Appl. Mater. Interfaces*, 2019, **11**(34), 30786–30792.

51 S. Ding, T. Dong, T. Peppel, N. Steinfeldt, J. Hu and J. Strunk, Construction of amorphous SiO_2 modified β-Bi_2O_3 porous hierarchical microspheres for photocatalytic antibiotics degradation, *J. Colloid Interface Sci.*, 2022, **607**, 1717–1729.

52 H. Sato, T. Minami, S. Takata and T. Yamada, Transparent conducting p-type NiO thin films prepared by magnetron sputtering, *Thin Solid Films*, 1993, **236**(1–2), 27–31.

53 M. C. Toroker, D. K. Kanan, N. Alidoust, L. Y. Isseroff, P. Liao and E. A. Carter, First principles scheme to evaluate band edge positions in potential transition metal oxide photocatalysts and photoelectrodes, *Phys. Chem. Chem. Phys.*, 2011, **13**(37), 16644–16654.

54 S. Linic, P. Christopher and D. B. Ingram, Plasmonic-metal nanostructures for efficient conversion of solar to chemical energy, *Nat. Mater.*, 2011, **10**(12), 911–921.

55 J. B. Priebe, M. Karnahl, H. Junge, M. Beller, D. Hollmann and A. Brückner, Water reduction with visible light: synergy between optical transitions and electron transfer in Au-TiO_2 catalysts visualized by in situ EPR spectroscopy, *Angew. Chem., Int. Ed.*, 2013, **52**(43), 11420–11424.

56 Z. Zhang, X. Wang, J. Long, Q. Gu, Z. Ding and X. Fu, Nitrogen-doped titanium dioxide visible light photocatalyst: spectroscopic identification of photoactive centers, *J. Catal.*, 2010, **276**(2), 201–214.

57 M. Okumura, J. M. Coronado, J. Soria, M. Haruta and J. C. Conesa, EPR study of CO and O_2 interaction with supported Au catalysts, *J. Catal.*, 2001, **203**(1), 168–174.

58 P. Claus, A. Brückner, C. Mohr and H. Hofmeister, Supported gold nanoparticles from quantum dot to mesoscopic size scale: Effect of electronic and structural properties on catalytic hydrogenation of conjugated functional groups, *J. Am. Chem. Soc.*, 2000, **122**(46), 11430–11439.

59 J. C. Wu and C.-W. Huang, In situ DRIFTS study of photocatalytic CO_2 reduction under UV irradiation, *Front. Chem. Eng. China*, 2010, **4**, 120–126.

60 C. Mu, C. Lv, X. Meng, J. Sun, Z. Tong and K. Huang, In situ characterization techniques applied in photocatalysis: a review, *Adv. Mater. Interfaces*, 2023, **10**(3), 2201842.

61 P. Naliwajko, T. Peppel and J. Strunk, Thermal and light induced infrared blackening of ZnO revisited: Rediscovery of fundamental scientific knowledge, *React. Kinet., Mech. Catal.*, 2022, **135**(5), 2291–2305.

This journal is © The Royal Society of Chemistry 2024

Catal. Sci. Technol., 2024, **14**, 3459–3472 | **3471**

62 X. Chang, T. Wang and J. Gong, CO_2 photo-reduction: insights into CO_2 activation and reaction on surfaces of photocatalysts, *Energy Environ. Sci.*, 2016, **9**(7), 2177–2196.

63 K. Bhattacharyya, A. Danon, K. B. Vijayan, K. A. Gray, P. C. Stair and E. Weitz, Role of the surface lewis acid and base sites in the adsorption of CO_2 on titania nanotubes and platinized titania nanotubes: an in situ FT-IR study, *J. Phys. Chem. C*, 2013, **117**(24), 12661–12678.

64 G. Martra, Lewis acid and base sites at the surface of microcrystalline TiO_2 anatase: relationships between surface morphology and chemical behaviour, *Appl. Catal., A*, 2000, **200**(1–2), 275–285.

65 W. Su, J. Zhang, Z. Feng, T. Chen, P. Ying and C. Li, Surface phases of TiO_2 nanoparticles studied by UV Raman spectroscopy and FT-IR spectroscopy, *J. Phys. Chem. C*, 2008, **112**(20), 7710–7716.

66 K. K. Bando, K. Sayama, H. Kusama, K. Okabe and H. Arakawa, In-situ FT-IR study on CO_2 hydrogenation over Cu catalysts supported on SiO_2, Al_2O_3, and TiO2, *Appl. Catal., A*, 1997, **165**(1–2), 391–409.

67 L.-F. Liao, C.-F. Lien, D.-L. Shieh, M.-T. Chen and J.-L. Lin, FTIR study of adsorption and photoassisted oxygen isotopic exchange of carbon monoxide, carbon dioxide, carbonate, and formate on TiO2, *J. Phys. Chem. B*, 2002, **106**(43), 11240–11245.

68 J. Rasko and F. Solymosi, Infrared spectroscopic study of the photoinduced activation of CO_2 on TiO_2 and Rh/TiO_2 catalysts, *J. Phys. Chem.*, 1994, **98**(29), 7147–7152.

69 J. Baltrusaitis, J. Schuttlefield, E. Zeitler and V. H. Grassian, Carbon dioxide adsorption on oxide nanoparticle surfaces, *Chem. Eng. J.*, 2011, **170**(2–3), 471–481.

70 L. Mino, G. Spoto and A. M. Ferrari, CO_2 capture by TiO_2 anatase surfaces: a combined DFT and FTIR study, *J. Phys. Chem. C*, 2014, **118**(43), 25016–25026.

71 D. Bernitt, K. Hartman and I. Hisatsune, Infrared spectra of isotopic bicarbonate monomer ions, *J. Chem. Phys.*, 1965, **42**(10), 3553–3558.

72 C.-C. Yang, Y.-H. Yu, B. van der Linden, J. C. Wu and G. Mul, Artificial photosynthesis over crystalline TiO_2-based catalysts: fact or fiction?, *J. Am. Chem. Soc.*, 2010, **132**(24), 8398–8406.

73 K. Li, S. Zhang, Q. Tan, X. Wu, Y. Li, Q. Li, J. Fan and K. Lv, Insulator in photocatalysis: Essential roles and activation strategies, *Chem. Eng. J.*, 2021, **426**, 130772.

74 S. Han, X. Li, Y. Tan, Y. Huang, Z. Wu, M. Wang, W. Ho and S.-C. Lee, In-situ self-sacrificed fabrication of insulator-based $SrTiO_3/SrCO_3$ heterojunction interface for gaseous HCHO

and NO photocatalytic degradation, *Appl. Surf. Sci.*, 2023, **612**, 155806.

75 R. Jacobs, J. Booske and D. Morgan, Understanding and controlling the work function of perovskite oxides using density functional theory, *Adv. Funct. Mater.*, 2016, **26**(30), 5471–5482.

76 K. H. Zhang, R. Wu, F. Tang, W. Li, F. E. Oropeza, L. Qiao, V. K. Lazarov, Y. Du, D. J. Payne and J. L. MacManus-Driscoll, Electronic structure and band alignment at the NiO and $SrTiO_3$ p–n heterojunctions, *ACS Appl. Mater. Interfaces*, 2017, **9**(31), 26549–26555.

77 K. Domen, A. Kudo and T. Onishi, Mechanism of photocatalytic decomposition of water into H_2 and O_2 over $NiO-SrTiO_3$, *J. Catal.*, 1986, **102**(1), 92–98.

78 S. A. Rawool, M. R. Pai, A. M. Banerjee, A. Arya, R. Ningthoujam, R. Tewari, R. Rao, B. Chalke, P. Ayyub and A. Tripathi, pn Heterojunctions in NiO: TiO_2 composites with type-II band alignment assisting sunlight driven photocatalytic H_2 generation, *Appl. Catal., B*, 2018, **221**, 443–458.

79 B. Sun, G. Zhou, T. Gao, H. Zhang and H. Yu, NiO nanosheet/TiO2 nanorod-constructed p–n heterostructures for improved photocatalytic activity, *Appl. Surf. Sci.*, 2016, **364**, 322–331.

80 A. Hezam, T. Peppel and J. Strunk, Pathways towards a systematic development of Z scheme photocatalysts for CO_2 reduction, *Curr. Opin. Green Sustainable Chem.*, 2023, 100789.

81 A. Pougin, G. Dodekatos, M. Dilla, H. Tüysüz and J. Strunk, Au@ TiO_2 core–shell composites for the photocatalytic reduction of CO_2, *Chem. – Eur. J.*, 2018, **24**(47), 12416–12425.

82 H. Shen, T. Peppel, J. Strunk and Z. Sun, Photocatalytic reduction of CO_2 by metal-free-based materials: recent advances and future perspective, *Sol. RRL*, 2020, **4**(8), 1900546.

83 K. Li, X. An, K. H. Park, M. Khraisheh and J. Tang, A critical review of CO_2 photoconversion: Catalysts and reactors, *Catal. Today*, 2014, **224**, 3–12.

84 K. Li, B. Peng and T. Peng, Recent advances in heterogeneous photocatalytic CO_2 conversion to solar fuels, *ACS Catal.*, 2016, **6**(11), 7485–7527.

85 L. Liao, G. Xie, X. Xie and N. Zhang, Advances in Modulating the Activity and Selectivity of Photocatalytic CO2 Reduction to Multicarbon Products, *J. Phys. Chem. C*, 2023, **127**(6), 2766–2781.

3472 | *Catal. Sci. Technol.*, 2024, **14**, 3459–3472

This journal is © The Royal Society of Chemistry 2024